

Serinv: A Scalable Library for the Selected Inversion of Block-Tridiagonal with Arrowhead Matrices

Vincent Maillou

D-ITET, ETH Zurich
Switzerland
vmaillou@iis.ee.ethz.ch

Lisa Gaedke-Merzhaeuser

Institute of Computing, USI, CH
CEMSE Division, Kaust, SA
lisa.gaedkemerzhauser@kaust.edu.sa

Alexandros Nikolaos Ziogas

D-ITET, ETH Zurich
Switzerland
alexandros.ziogas@iis.ee.ethz.ch

Olaf Schenk

Institute of Computing, USI
Switzerland
olaf.schenk@usi.ch

Mathieu Luisier

D-ITET, ETH Zurich
Switzerland
mluisier@iis.ee.ethz.ch

Abstract

The inversion of structured sparse matrices is a key but computationally and memory-intensive operation in many scientific applications. There are cases, however, where only particular entries of the full inverse are required. This has motivated the development of so-called *selected-inversion* algorithms, capable of computing only specific elements of the full inverse. Currently, most of them are either shared-memory codes or limited to CPU implementations. Here, we introduce *Serinv*, a scalable library providing distributed, GPU-based algorithms for the selected inversion and Cholesky decomposition of positive-definite, block-tridiagonal arrowhead matrices. This matrix class is highly relevant in statistical climate modeling and materials science applications. The performance of *Serinv* is demonstrated on synthetic and real datasets from statistical air temperature prediction models. In our numerical tests, *Serinv* achieves 32.3% strong and 47.2% weak scaling efficiency and up to two orders of magnitude speedup over the sparse direct solvers PARDISO and MUMPS on 16 GPUs.

CCS Concepts

• **Theory of computation** → **Distributed algorithms**; • **Mathematics of computing** → **Solvers**; • **Applied computing** → *Mathematics and statistics*.

Keywords

Selected inversion, Cholesky factorization, scalable algorithms, GPU implementation, structured sparse matrices

1 Introduction

Many applications in materials science, computational chemistry, or statistical modeling require inverting large sparse matrices [19, 35, 36, 50] with a structured pattern and extracting selected entries of their inverse, for example, the diagonal elements. Since matrix inversions generally lead to dense matrices, depending on the size of the problem at hand, such operations rapidly become unfeasible, either because of memory or timing constraints. When specific entries of the inverse are needed, it is advantageous to compute only the desired ones without considering the others. To achieve this, so-called *selected-inversion* algorithms [16, 24] have been derived to directly and exactly compute the desired elements of the inverse, thus speeding up the process and reducing the memory footprint.

HW/Sparsity	Unstructured	BT	BTA
Shared Memory	CPU MUMPS [†] [4–6] Pardiso [*] [9, 42–44] PSelInv [†] [30, 31] FIND [26–29]	RGF [†] [39, 47]	INLA [†] _{BTA} [17, 18]
	GPU	RGF [†] [51]	INLA [†] _{BTA} [17, 18]
Distributed Memory	CPU MUMPS [†] [4–6]	Serinv [†] PSR [38] P-DIV/Spikes [12, 13, 40, 46] BCR [10, 23]	Serinv [†]
	GPU	Serinv [†] SplitSolve [11] P-DIV/Spikes [48]	Serinv [†]

Table 1: Summary of existing selected-inversion algorithms, sorted by hardware (shared- and distributed-memory, CPUs, and GPUs) and sparse matrices type support (unstructured, BT, and BTA). We denote with a [†] (*) the open-source (closed-license) packages. Algorithms without annotation do not have any publicly available implementation to our knowledge. This work’s contribution, *Serinv*, is highlighted in cyan.

Selected inversion lends itself particularly well to Bayesian inference problems relying on integrated nested Laplace approximations (INLA) [41]. The latter provides approximate inference estimates for latent Gaussian models (LGMs). To save memory, such models can be described using sparse precision matrices, which typically possess well-structured sparsity patterns. Block tridiagonal (BT) and block tridiagonal arrowhead (BTA) structures are very common in INLA [32]. To estimate the required marginal variances of latent parameters, selected entries of the precision matrix’s inverse, i.e., its covariance matrix, must be extracted.

Selected-inversion algorithms rely on an appropriate decomposition of the matrix of interest, for example, via LU or Cholesky factorization. In the case of sparse matrices, the fill-in caused by these operations, i.e., zero entries of the matrix overwritten by non-zeros elements, represents a significant challenge as it increases the overall memory footprint and computational cost. This is particularly true for *unstructured* matrices, where the coordinates of the non-zero entries do not follow any particular pattern.

Therefore, the decomposition and selected inversion of unstructured matrices necessitate algorithms oblivious to the distribution of the non-zero elements. In matrices with a *structured* (predefined) sparsity pattern, the locations where non-zeros may appear during

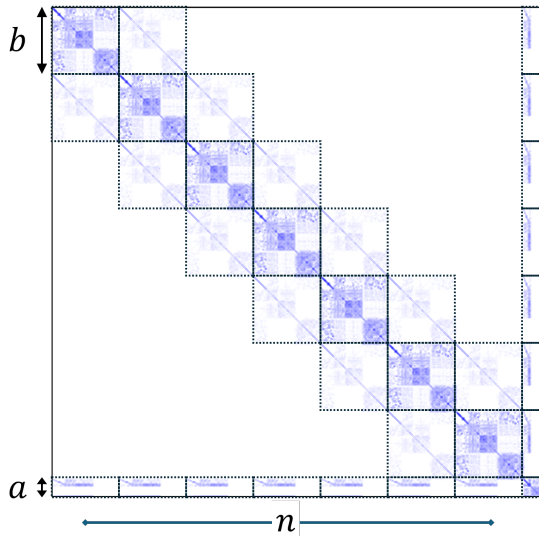


Figure 1: Symmetric, positive-definite, block-tridiagonal arrowhead (BTA) matrix resulting from statistical modeling applied to temperature prediction. The data was discretized on a 7-day time grid. The matrix is described by the number of main diagonal blocks n , their size b , and the arrow tip block size a .

the decomposition phase are limited, providing unique opportunities for optimization [20].

Of particular interest are structured matrices whose decomposition induced fill-in remains within the bound of their sparsity pattern.

The aforementioned BT and BTA matrices fulfill this property. They naturally appear in the quantum transport simulations of nanoscale materials and devices [35, 36] or INLA-based statistical climate modeling problems [18]. Alternatively, they can be constructed from unstructured matrices through decomposition and permutation [8, 21]. By taking advantage of the BT and BTA sparsity patterns, the computational cost and memory footprint of selected-inversion and decomposition methods can be greatly reduced, typically from $O(N^3)$ down to $O(n \times b^3)$ [39, 51], where $N = n \times b$ is the original system size, while n is the number of diagonal blocks and b their size.

There are four types of selected-inversion algorithms (SIA):

1.0.1 Decomposition-based SIA. rely on an appropriate factorization of the initial matrix. They can be applied to both unstructured and block-structured sparse matrices. In the literature, they are referred to as *Takahashi* SIA. Our methods belong to this category.

1.0.2 Schur complement-based SIA. take advantage of the iterative (or recursive) calculation of the Schur complement of the matrix to be inverted. They have attracted wide attention from the device modeling community due to their simplicity and capability to embed the solution of an equation of form $AXA^\dagger = B$ alongside the selected inversion of A [39, 47].

1.0.3 Sherman-Morrison-Woodbury (SMW)-based SIA. use a divide-and-conquer approach to update the independent partitions of the matrix of interest with the SMW formula. They are at the core of the *SPIKE* algorithm and its derivatives [11–13, 40, 46, 48]. SMW-based SIA are very similar to the Schur-complement ones.

1.0.4 Block cyclic reduction (BCR)-based SIA. combine a BCR and production phase to compute the SI of a BT matrix in a divide-and-conquer fashion. They have been extensively studied to solve tridiagonal systems of equations [10, 23] and their block variants. Because the BCR phase presents a higher complexity than typical decomposition algorithms, it limits the practical relevance of this approach.

Current implementations of selected-inversion algorithms are either restricted to shared- and distributed-memory CPU architectures [4–6, 30, 31, 38, 47, 51] or to single GPUs [18], as summarized in Table 1. As such, they do not allow for the handling of large matrices and hinder the investigation of realistic physical systems. Also, the algorithms targeting unstructured matrices generally perform sub-optimally when dealing with BT or BTA matrices. Hence, dedicated approaches have been developed for these matrix types. However, distributed-memory schemes only exist for the BT sparsity pattern, not for the BTA one [23, 38, 40].

Here, we go one step further and present distributed-memory, selected-inversion algorithms for positive semi-definite BTA matrices. Our approach is based on a block-Cholesky decomposition and selected inversion of BTA matrices. It is implemented in a scalable library called *Serinv*, which is adapted to CPU as well as GPU architectures. Our innovations are highlighted in cyan in Table 1. *Serinv* bridges the remaining gap between the BTA structured sparsity pattern and modern, GPU-accelerated, distributed-memory algorithms. We provide a theoretical analysis of our method and experimental results on CPU and GPU, on shared- and distributed-memory systems. Our new approach surpasses state-of-art, where we exhibit up to 2.6x (resp. 71.4x) speedup on CPU (resp. GPU) over PARDISO and 14.0x (resp. 380.9x) speedup over MUMPS when scaling to 16 processes. We achieve 32.3% strong and 47.2% weak scaling efficiency when going from 1 to 16 GPUs.

The main contributions of this work are the following:

- Derivation of distributed Cholesky decomposition and SIA for positive semi-definite BTA matrices;
- Distributed-memory implementation of these algorithms for BTA matrices on CPU and GPU;
- Theoretical complexity analysis of the proposed methods;
- Comparison with the state-of-the-art sparse solvers PARDISO and MUMPS on real-world datasets;
- Demonstration of strong and weak scaling of the selected-inversion algorithms.

The paper is organized as follows: In Section 2, we introduce the required mathematical and algorithmic background. Our new algorithms are presented in Section 3 before conducting a theoretical analysis in Section 4. We discuss our numerical results for the sequential and distributed codes in Section 5. Finally, conclusions are drawn in Section 6.

Name	Description
n	Number of square blocks in a BTA matrix's main block diagonal, excluding the arrow tip block.
b	Size of the square blocks in a BTA matrix's main, upper, and lower block diagonals, excluding the arrowhead blocks.
a	Size of the arrow tip block.
N	Total size of the BTA matrix, equal to $nb + a$.
P	Number of parallel processes and matrix partitions.
Block-Sequential	Refers to algorithms and routines expressed in matrix-block operations with <i>sequential</i> dependencies among them.
Forward Pass	Block-sequential for-loop operating from the top-left blocks of (the partition of) a matrix towards the bottom-right ones.
Backward Pass	Block-sequential for-loop operating from the bottom-right blocks of (the partition of) a matrix towards the top-left ones.
True Inverse	Refers to the blocks of a matrix's selected inverse, distinct from any transient or temporary results.
PO	Positive-definite matrix.
BTA	Block tridiagonal arrowhead matrix.
F	Factorization.
I	Inversion.
SIA	Selected-inversion algorithm.
P	Parallel algorithm.
PARTIAL	Refers to an algorithm that only performs a restricted set of its normal operations.
PERMUTED	Refers to an algorithm acting on middle (permuted) partitions of a BTA matrix.

Table 2: Symbols and terms used in this work.

Algorithm 1 *POBTAF*: Block-sequential block-Cholesky factorization of a BTA matrix.

Input: A : BTA matrix.

Output: L : Lower-triangular factor.

```

1: for  $i = 0; i < n - 1; i++$  do
2:    $L_{i,i} \leftarrow \text{POTRF}(A_{i,i})$ 
3:    $L_{i+1,i} \leftarrow \text{TRSM}(L_{i,i}, A_{i+1,i})$ 
4:    $L_{n,i} \leftarrow \text{TRSM}(L_{i,i}, A_{n,i})$ 
5:    $A_{i+1,i+1} \leftarrow A_{i+1,i+1} - L_{i+1,i} \times L_{i+1,i}^\dagger$ 
6:    $A_{n,i+1} \leftarrow A_{n,i+1} - L_{n,i} \times L_{i+1,i}^\dagger$ 
7:    $A_{n,n} \leftarrow A_{n,n} - L_{n,i} \times L_{n,i}^\dagger$ 
8: end for
9:  $L_{n-1,n-1} \leftarrow \text{POTRF}(A_{n-1,n-1})$ 
10:  $L_{n,n-1} \leftarrow \text{TRSM}(L_{n-1,n-1}, A_{n,n-1})$ 
11:  $A_{n,n} \leftarrow A_{n,n} - L_{n,n-1} \times L_{n,n-1}^\dagger$ 
12:  $L_{n,n} \leftarrow \text{POTRF}(A_{n,n})$ 

```

2 Background

This section presents the notation and terminology used throughout the paper. A summary is given in Table 2. Subsequently, we describe the current state-of-the-art methods for the selected inversion of BTA matrices.

2.1 Notation and terminology

In this work, we focus on BTA matrices with a sparsity pattern similar to Fig. 1. A BTA matrix comprises three block diagonals (main, upper, and lower) and an arrowhead consisting of the last (by convention) block row and block column. We use the term *arrow tip* for the block at the intersection of the arrowhead's block row and column. Elements within the arrowhead usually embed properties shared by (or connecting) all interacting elements in the model. The BTA matrix's main block diagonal consists of n square blocks of size b , while the arrow tip has size a . The rest of the arrowhead blocks are rectangular with size $a \times b$ or $b \times a$. The total size of the

Algorithm 2 *POBTASI*: Block-sequential selected inversion of a BTA matrix, given its block-Cholesky decomposition.

Input: L : Lower-triangular factor.

Output: X : Selected inverse of A .

```

1:  $X_{n,n} \leftarrow L_{n,n}^{-\dagger} \times L_{n,n}^{-1}$ 
2:  $U_{n,n-1} \leftarrow -X_{n,n} \times L_{n,n-1}$ 
3:  $X_{n,n-1} \leftarrow \text{TRSM}(L_{n-1,n-1}, U_{n,n-1})$ 
4:  $U_{n-1,n-1} \leftarrow L_{n-1,n-1}^{-\dagger} - X_{n,n-1}^\dagger \times L_{n,n-1}$ 
5:  $X_{n-1,n-1} \leftarrow \text{TRSM}(L_{n-1,n-1}, U_{n-1,n-1})$ 
6: for  $i = n - 2; i \geq 0; i--$  do
7:    $U_{i+1,i} \leftarrow -X_{i+1,i+1} \times L_{i+1,i} - X_{n,i+1}^\dagger \times L_{n,i}$ 
8:    $X_{i+1,i} \leftarrow \text{TRSM}(L_{i,i}, U_{i+1,i})$ 
9:    $U_{n,i} \leftarrow -X_{n,i+1} \times L_{i+1,i} - X_{n,n} \times L_{n,i}$ 
10:   $X_{n,i} \leftarrow \text{TRSM}(L_{i,i}, U_{n,i})$ 
11:   $U_{i,i} \leftarrow L_{i,i}^{-\dagger} - X_{i+1,i}^\dagger \times L_{i+1,i} - X_{n,i}^\dagger \times L_{n,i}$ 
12:   $X_{i,i} \leftarrow \text{TRSM}(L_{i,i}, U_{i,i})$ 
13: end for

```

matrix N is equal to $nb + a$. We note that BTA matrices can be seen as a generalization of the BT sparsity pattern. Indeed, a BT matrix is BTA with $a = 0$.

While BTA matrices are ubiquitous in many fields, we focus on those arising from spatio-temporal statistical models for temperature prediction. Fig. 1 depicts a precision matrix generated using a stochastic partial differential equations approach [33] from statistical modeling. The main diagonal blocks of the matrix correspond to the spatial discretization of the simulated domains using a finite-element method at different time steps, which are coupled through the upper and lower diagonal blocks. While the block tridiagonal part of the matrix, relates to local phenomena, the arrowhead component accounts for global effects in the model. For example, in the case of a temperature prediction model, the arrowhead component could encode information on the elevation of different space-time variables, which is assumed to affect the temperature independently of the exact time and space location.

Since the matrices describing such problems are symmetric positive-definite, we focus on selected inversion through lower-triangular block-Cholesky factorization [34]. However, all algorithms presented here have a straightforward extension to general BTA matrices using block-LU decomposition, provided they exhibit certain properties, such as block-diagonal dominance [15]. This is a common case in materials sciences.

All our methods rely on block algorithms and use BLAS and LAPACK operations. We refer to those methods or subroutines that exhibit *sequential* data dependencies among the block-level operations as *block-sequential*. These methods apply to matrices that can grow very large, rendering them amenable to asymptotic analysis. However, the block sizes a and b are finite and relatively small ($\approx 100 - 10,000$) in practical applications. Therefore, considering the cost of distributed-memory communication in modern architectures, block-level parallelism may only be fruitfully exploited in shared memory. The block-sequential algorithms typically consist of block-sequential for-loops called either *forward* or *backward* passes. A forward pass, by convention, operates *sequentially* from the top-left blocks of a matrix (or a matrix's partition, in the case of distributed-memory algorithms) towards the bottom-right ones. A

backward pass goes in the opposite direction. The overall selected-inversion process produces intermediate results, and certain matrix blocks may be updated several times, especially in the case of in-place and distributed-memory implementations. To distinguish between those transient results and the final output, we describe blocks of the inverse as *true inverse*.

We follow a BLAS- and LAPACK-like naming scheme for the methods' names. In the LAPACK routines *POTRF* and *POTRI*, "PO" stands for positive-definite matrix, "TR" for triangular matrix, "F" for factorization, and "I" for inversion. Thus, we call the Cholesky factorization of a BTA matrix *POBTAF* and its selected inversion *POBTASI*. We use the "SI" string to explicitly distinguish selected inversion from regular full inversion. In the case of distributed-memory algorithms, we prepend "P" to the routine names, similarly to PBLAS and ScaLAPACK. We also use P to define the total number of parallel processes and partitions. Finally, we use the "PERMUTED" string to refer to an algorithm operating on a BTA matrix's permutation or slice.

2.2 Block-sequential selected inversion of BTA matrices

The Cholesky decomposition of a symmetric, positive-definite, matrix A is a lower (upper) triangular matrix L (U) such that $A = LL^T$ ($A = U^T U$). Algorithm 1 presents *POBTAF*, the block-sequential method for the block-Cholesky factorization of BTA matrices. It is implemented in the `INLABTA` subcomponent of the `INLADIST` package [18]. This algorithm executes a forward pass and, in each iteration, computes the lower-triangular Cholesky decomposition $L_{i,i}$ of the corresponding main diagonal block using LAPACK's *POTRF* routine. The computed main diagonal factor $L_{i,i}$ is then used to determine the lower diagonal $L_{i+1,i}$ and arrowhead $L_{n,i}$ factors, which lie in the same block column. After evaluating those factors, *POBTAF* performs a forward update of the next main diagonal and arrowhead blocks, $A_{i+1,i+1}$ and $A_{n,i+1}$. It also updates the arrow tip $A_{n,n}$.

Algorithm 2 introduces *POBTASI*, a block-sequential method for the block-selected inversion of BTA matrices, given their block-Cholesky factorization. It is also available in the `INLABTA` package [18]. *POBTASI* computes A^{-1} 's true inverse blocks with the exact same coordinates as the non-zero blocks of A . The algorithm performs a backward pass, iterating over the block rows of A , while computing the true inverse lower diagonal and arrowhead blocks, $X_{i+1,i}$ and $X_{n,i}$. Both blocks are then used to produce the next main diagonal block of the selected inverse, $X_{i,i}$. *POBTASI* is derived from the Takahashi selected-inversion method for general sparse matrices [24], and, if desired, can be amended to compute more entries of the inverse A^{-1} than the number of non-zeros in A .

3 Methods

To break the data dependencies of the block-sequential algorithms presented in Section 2.2, we introduce a permutation scheme extending the work of Petersen et al. [38]. Applying this permutation to the input matrix allows us to reorder the block operations, exposing parallel sections in the forward and backward passes. Overall, the algorithm we propose splits the input matrix A into P partitions and comprises three phases: (1) *PPOBTAF* computes

partial block-Cholesky factorizations for all partitions in parallel. (2) *POBTARSSI* gathers the partial factorizations' blocks lying in the boundaries among the partitions to construct a smaller BTA matrix called *reduced system* and labeled A_r . The method then computes the reduced system's selected inverse by sequentially applying the *POBTAF* and *POBTASI* methods. The selected inverse of the reduced-system, X_r , consists of the true inverse boundary blocks of each partition. (3) *PPOBTASI* uses the latter blocks to execute the backward pass of Algorithm 2 for all partitions in parallel, which delivers selected entries of A^{-1} .

3.1 Partitioning and permutation schemes

We partition the BTA matrix into P disjoint arrow shapes, each consisting (approximately) of $n_p = n/P$ block rows and columns. The coordinates of the blocks belonging to a partition p are $A_{i,i}$ (main block diagonal), $A_{i+1,i}$ (lower block diagonal), and $A_{n,i}$ (arrowhead) for $i \in \{pn_p..(p+1)n_p - 1\}$. We distinguish between the first (top) partition p_0 , which owns block $A_{0,0}$, and the rest, *middle* partitions. All partitions share the arrow tip block $A_{n,n}$ and can then be re-interpreted as a BTA matrix with $n = n_p$. An example BTA matrix, with $n = 11$, split into three partitions is shown, alongside its permutation matrix, in Fig. 2.

The matrix P can be defined as a *shifting* permutation, re-organizing the blocks inside the sparsity structure. In practice, applying this permutation matrix to a BTA partition shifts its blocks up and left along the diagonal. The first diagonal block belonging to this partition is shifted around to the last position. For example, in Fig. 2, the first diagonal block of partition 1 is $A_{3,3}$. After applying the permutation, the first diagonal block is $A_{4,4}$, while $A_{3,3}$ is shifted around to the last position. This permutation is necessary to factorize the middle partitions toward their two neighboring partitions, above and below, allowing for further completion of the partial factorization during the *POBTARSSI* step. The blocks connecting the partitions, represented in dark gray color in Fig. 2, remain untouched during the permutation. These blocks are later going to be used to connect the partitions together when assembling the reduced system at the end of the parallel factorization phase. The middle partitions' permutation induces fill-in during the partial block-Cholesky factorization, annotated with red hatches in the permuted matrix in Fig. 2. Due to this fill-in, the *PPOBTAF* and *PPOBTASI* methods execute more block operations for the middle partitions than for the first one. Load balancing issues are further discussed in Section 4. We note that the permutation is never materialized but remains implicit, i.e., the blocks of A and L are not reordered in memory.

3.2 Parallel partial BTA block-Cholesky factorization

The first step in our parallel selected-inversion algorithm is to produce a partial block-Cholesky factorization of the initial BTA matrix. To that end, we split the input into P partitions using the scheme presented in Section 3.1, one top partition, and $P - 1$ middle partitions. The factorizations' computations are independent and, therefore, we can employ P processes in parallel, as shown in Algorithm 3. We use different block-sequential algorithms for the top (*PARTIAL_POBTAF*) and middle partitions (*PERMUTED_POBTAF*).

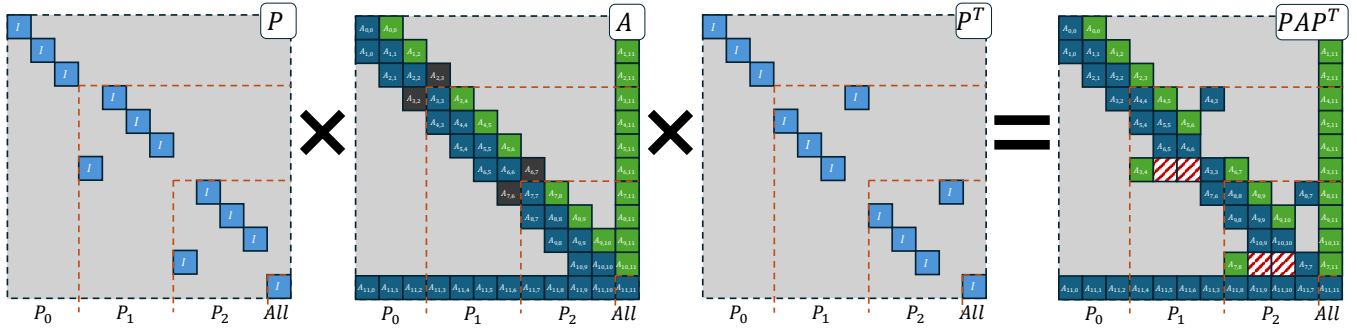


Figure 2: Permutation scheme applied on a symmetric, positive-definite, matrix in order to perform its parallel factorization and selected-inversion. The matrix is distributed amongst three processes and permuted accordingly. The permutation-induced fill-in during the decomposition is shown in red hatches in the permuted matrix.

Algorithm 3 PPOBTAF: Parallel block-Cholesky factorization of a BTA matrix.

Input: $A_{p_i}, i \in \{0, \dots, P-1\}$: P partitions of A .

Output: $L_{p_i}, i \in \{0, \dots, P-1\}$: P partitions of L .

Output: $B_{p_i}, i \in \{1, \dots, P-1\}$: $P-1$ fill-in partitions.

```

1: for all  $i \in \{0, \dots, P-1\}$  do
2:   if  $i == 0$  then
3:      $(L_{p_0}, U_{p_0}) \leftarrow \text{PARTIAL\_POBTAF}(A_{p_0})$ 
4:   else
5:      $(L_{p_i}, B_{p_i}, U_{p_i}) \leftarrow \text{PERMUTED\_POBTAF}(A_{p_i})$ 
6:   end if
7: end for
8:  $L_{n,n} \leftarrow A_{n,n} + \sum_{i=0}^{P-1} U_{p_i}$ 

```

Algorithm 4 PERMUTED_POBTAF: Block-sequential partial block-Cholesky factorization of a middle BTA partition. Differences compared to POBTAF are highlighted in red.

Input: A : Middle partition with n_p main diagonal blocks.

Output: L : Middle lower-triangular factor partition.

Output: B : Permutation-induced fill-in.

Output: U_{tip} : Partial arrow tip update.

```

1:  $B_1 = A_{1,0}^\dagger, U_{tip} = 0$ 
2: for  $i = 1; i < n_p - 1; i++$  do
3:    $L_{i,i} \leftarrow \text{POTRF}(A_{i,i})$ 
4:    $L_{i+1,i} \leftarrow \text{TRSM}(L_{i,i}, A_{i+1,i})$ 
5:    $L_{n_p,i} \leftarrow \text{TRSM}(L_{i,i}, A_{n_p,i})$ 
6:    $B_i \leftarrow \text{TRSM}(L_{i,i}, B_i)$ 
7:    $A_{i+1,i+1} \leftarrow A_{i+1,i+1} - L_{i+1,i} \times L_{i+1,i}^\dagger$ 
8:    $A_{n_p,i+1} \leftarrow A_{n_p,i+1} - L_{n_p,i} \times L_{i+1,i}^\dagger$ 
9:    $U_{tip} \leftarrow U_{tip} - L_{n_p,i} \times L_{n_p,i}^\dagger$ 
10:   $A_{0,0} \leftarrow A_{0,0} - B_i \times B_i^\dagger$ 
11:   $B_{i+1} \leftarrow -B_i \times L_{i+1,i}^\dagger$ 
12:   $A_{n_p,0} \leftarrow A_{n_p,0} - L_{n_p,i} \times B_i^\dagger$ 
13: end for

```

Both routines are variations of POBTAF, specifically lines 1–8. The main difference is that, instead of updating the arrow tip block at each step, the update is accumulated in a buffer U_{tip} . At the end

Algorithm 5 PPOBTASI: Parallel selected inversion of a BTA matrix, given its block-Cholesky factorization.

Input: $L_{p_i}, i \in \{0, \dots, P-1\}$: P partitions of L .

Input: $B_{p_i}, i \in \{1, \dots, P-1\}$: $P-1$ fill-in partitions.

Output: $X_{p_i}, i \in \{0, \dots, P-1\}$: P partitions of X .

```

1: for all  $i \in \{0, \dots, P-1\}$  do
2:   if  $i == 0$  then
3:      $X_{p_0} \leftarrow \text{PARTIAL\_POBTASI}(L_{p_0})$ 
4:   else
5:      $X_{p_i} \leftarrow \text{PERMUTED\_POBTASI}(L_{p_i}, B_{p_i})$ 
6:   end if
7: end for

```

of the decomposition, the buffers from all partitions are added together. In addition to the normal operations arising in the partial factorization, the permuted factorization needs to compute extra blocks during the factorization. After applying the permutation scheme, the lower (resp. upper) blocks connecting the first diagonal block of the partition to the next one are shifted at the extremity of the partition. For example, in Fig. 2 and after application of the permutation matrix, the block $A_{4,3}$ (resp. $A_{3,4}$) that was initially within the BTA pattern is shifted outside of it, leading to the fill-in hatched in red during the factorization phase. These additional computations are performed in Algorithm 4 and Algorithm 6 using the buffer B_i . The differences compared to POBTAF are highlighted in red.

3.3 Reduced system and its selected inversion

Performing the partition-independent factorization of the matrix comes at the cost of solving an adjoint set of linear equations, i.e., a reduced system connecting the partitions. This reduced system, A_r , presents the same sparsity pattern as the initial matrix A but with fewer blocks. The number of blocks in the main diagonal of A_r is $n_r = 2P - 1$. The construction of this system from the blocks lying at the boundary among the partitions (brown color) is shown in Fig. 3.b) and c). A_r is solved with selected inversion, and the procedure is referred to as POBTARSSI. This operation can be implemented either using the block-sequential selected-inversion algorithms (POBTAF and POBTASI) or by applying our parallel process (PPOBTAF, POBTARSSI, and PPOBTASI), potentially in a

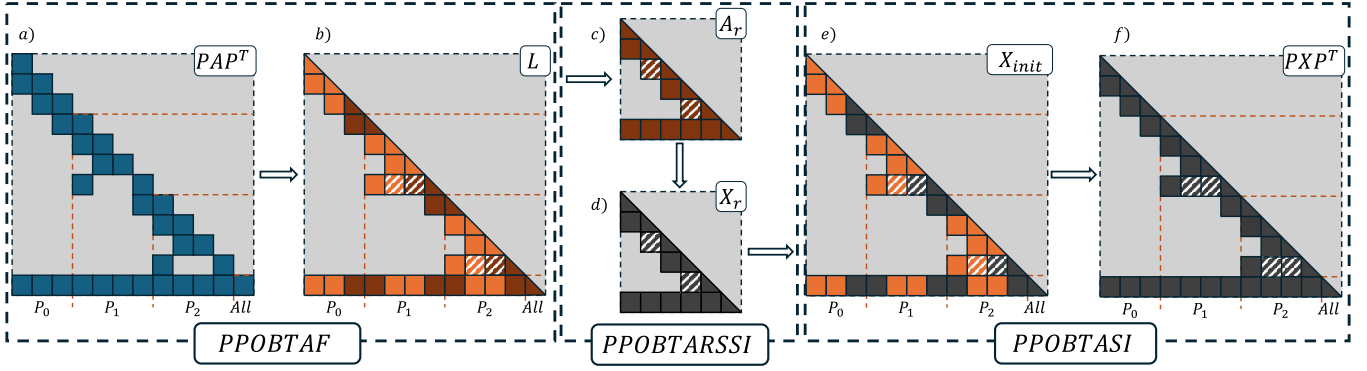


Figure 3: General organization of the distributed block-Cholesky factorization and selected inversion of a positive-definite BTA matrix. The method consists of three steps. a) and b) Parallel block-Cholesky factorization. c) and d) Creation of the reduced system A_r and its selected inversion X_r . e) and f) Parallel selected inversion.

Algorithm 6 *PERMUTED_POBTASI*: Block-sequential selected inversion of a middle BTA partition, given its block-Cholesky decomposition. Differences compared to POBTASI are highlighted in red.

Input: L : Middle lower-triangular factor partition.

Input: B : Permutation-induced fill-in.

Output: X : Middle partition with n_p main diagonal blocks.

```

1: for  $i = n_p - 2; i > 0; i--$  do
2:    $U_{i+1,i} \leftarrow -X_{i+1,i+1} \times L_{i+1,i} - X_{n_p,i+1}^\dagger \times L_{n_p,i}$ 
3:    $U_{i+1,i} \leftarrow U_{i+1,i} - B_{i+1}^\dagger \times B_i$ 
4:    $X_{i+1,i} \leftarrow \text{TRSM}(L_{i,i}, U_{i+1,i})$ 
5:    $V_i \leftarrow -B_{i+1} \times L_{i+1,i} - X_{0,0} \times B_i - X_{n_p,0}^\dagger \times L_{n_p,i}$ 
6:    $B_i \leftarrow \text{TRSM}(L_{i,i}, V_i)$ 
7:    $U_{n_p,i} \leftarrow -X_{n_p,i+1} \times L_{i+1,i} - X_{n_p,n_p} \times L_{n_p,i}$ 
8:    $U_{n_p,i} \leftarrow U_{n_p,i} - X_{n,0} \times L_{0,i}$ 
9:    $X_{n_p,i} \leftarrow \text{TRSM}(L_{i,i}, U_{n_p,i})$ 
10:   $U_{i,i} \leftarrow L_{i,i}^{-\dagger} \times -X_{i+1,i}^\dagger \times L_{i+1,i} - X_{n_p,i}^\dagger \times L_{n,i}$ 
11:   $U_{i,i} \leftarrow U_{i,i} - B_i^\dagger \times B_i$ 
12:   $X_{i,i} \leftarrow \text{TRSM}(L_{i,i}, U_{i,i})$ 
13: end for

```

recursive manner. The latter approach leads to the nested-solving method discussed in Section 4.2. The reduced system's selected inverse, X_r , consists of the true inverse blocks lying at the boundary among the partitions (dark gray color), as shown in Fig. 3.d) and e).

3.4 Parallel selected inversion of BTA matrices

Algorithm 5 describes the parallel selected inversion of a BTA matrix. POBTARSSI's result is copied to PPOBTASI's L and B inputs, as illustrated in Fig. 3.d) and e) in dark gray. The selected inversion of each partition can be computed independently of the others, and we can employ P processes in parallel. Similarly to PPOBTAF, we use different block-sequential algorithms for the top and middle partitions, *PARTIAL_POBTASI* and *PERMUTED_POBTASI*, respectively. Both routines are derived from POBTASI, specifically lines 6–13. The middle partitions must execute more block operations due to the permutation-induced fill-in B , highlighted in red in Algorithm 6. Figure 3 outlines the entire procedure from the parallel factorization of the initial BTA matrix (represented as permuted)

to the construction and selected inversion of the reduced system and, finally, its parallel selected inversion.

4 Theoretical analysis

In this section, we analyze the block-sequential and parallel algorithms derived in the previous sections. In Table 3, we present the BLAS and LAPACK routines used to operate on the dense blocks of the BTA matrices. Our algorithms rely on three routines, POTRF, GEMM, and TRSM, whose complexity is a function of the diagonal and arrow tip block sizes b and a . Table 3 further lists the number of calls of those three routines per method introduced in Sections 2.2, 3.2, 3.3, and 3.4. The given block-operation count for POBTARSSI corresponds to a block-sequential implementation (POBTAF and POBTASI) executed by a single process. We note that the parallel methods' GEMM and TRSM counts follow our implementation discussed in Section 5.1, where we have applied an optimization compared to Algorithms 3 and 5. Concretely, these algorithms call TRSM multiple times with the same lower-triangular factor $L_{i,i}$. Due to the performance characteristics of the TRSM and GEMM kernels executed on state-of-the-art GPU accelerators, it is beneficial to invert $L_{i,i}$ once and substitute the subsequent TRSM calls with GEMM operations. We further discuss the *practical* performance of those kernels in Section 5.3.1.

4.1 Computational complexity

Both block-sequential algorithms, POBTAF and POBTASI, exhibit the same asymptotic complexity with respect to the BTA matrix parameters a , b , and n : $O(nb^3)$ for sufficiently large n and under the assumption $a \leq b$. The most important constant factors are 3 and 2 for POBTAF and POBTASI, respectively. Similarly, the cost per process for the corresponding parallel algorithms is $O((n/p)b^3)$ with the same constant factors. However, the block-sequential POBTARSSI has complexity $O(Pb^3)$ with constant factor 20, inducing a work-depth trade-off to the full parallel selected-inversion algorithm. The total work is $O((n+P)b^3)$. Ignoring the b^3 factor, the depth is $O(n/p + P)$, limiting scaling.

Routine	Description	Complexity	Block-Operation Count				
			POBTAF	POBTASI	PPOBTAF	POBTARSSI	PPOBTASI
POTRF	Cholesky	$O(a^3)$	1	0	0	1	0
	Decomposition	$O(b^3)$	n	0	$n/P - 2$	$2P - 1$	0
GEMM	General Matrix-Matrix Multiplication	$O(a^3)$	0	1	0	1	0
		$O(a^2b)$	n	$n - 1$	$n/P - 2$	$4P - 3$	$n/P - 2$
		$O(ab^2)$	$n - 1$	$n - 1$	$n/P - 2$	$4P - 4$	$n/P - 2$
		$O(b^3)$	$n - 1$	$n - 1$	$n/P - 2$	$4P - 4$	$n/P - 2$
TRSM	Triangular	$O(ab^2)$	n	1	$n/P - 2$	$2P$	0
	Solve	$O(b^3)$	$n - 1$	$n - 1$	$n/P - 2$	$4P - 4$	$n/P - 2$

Table 3: Complexity of the BLAS and LAPACK routines used to perform Cholesky decomposition (POTRF), matrix-matrix multiplication (GEMM), and triangular solve (TRSM). a is the size of the arrow tip block, b is the size of main and lower diagonal blocks, while the rest of the arrowhead blocks have size $a \times b$ or $b \times a$. We also list the number of times each of these functions is called in routines for selected inversion of BTA matrices: POBTAF (block-sequential Cholesky factorization), POBTASI (block-sequential selected inversion), PPOBTAF (parallel Cholesky factorization), POBTARSSI (reduced system selected inversion), and PPOBTASI (parallel selected inversion). The counts of operations match the implementation made in the *Serinv* library and not necessarily the algorithmic listings.

4.2 Nested solving

Instead of executing POBTARSSI block sequentially, we can invert the reduced system using the developed parallel procedure. We note that we have to employ a subset of the processes, as this approach always leads to another reduced system $A_{r_{ns}}$ with $2P_{ns} - 1$ main diagonal blocks, where P_{ns} is the number of *nested-solving* processes. If $P_{ns} = P/c$ for a constant c , the algorithmic depth reduces from $O(n/P + P)$ to $O(n/P + P/c + c)$. The depth can be further decreased by using the nested-solving approach recursively. However, every recursive call increases communication volume and, especially, latency. Therefore, a proper theoretical evaluation of recursive nested solving must include a communication model. In this work, we limit our exploration to calling nested solving only once, using half the processes without modeling communication.

To highlight the scaling potential in more concrete terms, we restrict the values of the parameters describing a BTA matrix. Although n can grow arbitrarily large in typical scientific problems described by BTA matrices, the same is not true for a and b , which usually have values in the range of 1 – 500 for a and 100–10,000 for b , frequently on the lower side. For the rest of this section, we therefore fix a and b to 256 and 1024, respectively.

4.3 Load balancing

As discussed in Section 3.1, the middle processes perform more work due to the permutation fill-in, causing workload imbalances. To address this issue, the top partition’s size can be increased. To find the optimal ratio between the size of the top (n_{p_0}) and middle partitions (n_{p_i}), i.e., $r_{LB} = n_{p_0}/n_{p_i}$, we analyze in Table 4 the ideal workload balance given the floating-point operation count ratio between the block-sequential and parallel algorithms. Since the ideal load balancing factor differs for the factorization and

selected-inversion algorithms, we weight it according to the ratio of operations between the PPOBTAF and PPOBTASI routines. We report the load balancing factor for several values of n , ranging from 32 to 512, and find that it remains close to 2.25 in all cases.

4.4 Parallel efficiency

Using the floating-point operation counts for the block-sequential and parallel algorithms from Table 3 and the ideal load balancing ratios from Table 4, we present in Fig. 4.a) the theoretical maximum parallel efficiency of the entire parallel selected-inversion procedure (i.e., PPOBTAF + block-sequential POBTARSSI + PPOBTASI), for P ranging from 1 to 32 and n from 32 to 512. For every data point, we show the workload per process in TFLOP in parentheses and compute the efficiency as its ratio to the block-sequential workload for the same n value. The highest efficiency per process count is obtained for the maximal number of diagonal blocks $n = 512$, where

Number of blocks	32	64	128	256	512
Load balancing PPOBTAF	1.79	1.83	1.84	1.85	1.86
Load balancing PPOBTASI	2.43	2.45	2.46	2.46	2.46
Ratio PPOBTAF/PPOBTASI	0.34	0.34	0.35	0.35	0.35
Ideal load balancing (r_{LB})	2.22	2.24	2.24	2.25	2.25

Table 4: Load balancing factor r_{LB} between the partitions assigned to the *top* and the *middle* processes as a function of the number of blocks in the matrix. The reported values are obtained by first computing the load balancing between these partitions for the PPOBTAF and PPOBTASI routines and then by weighting the results with the number of operations performed for each function.

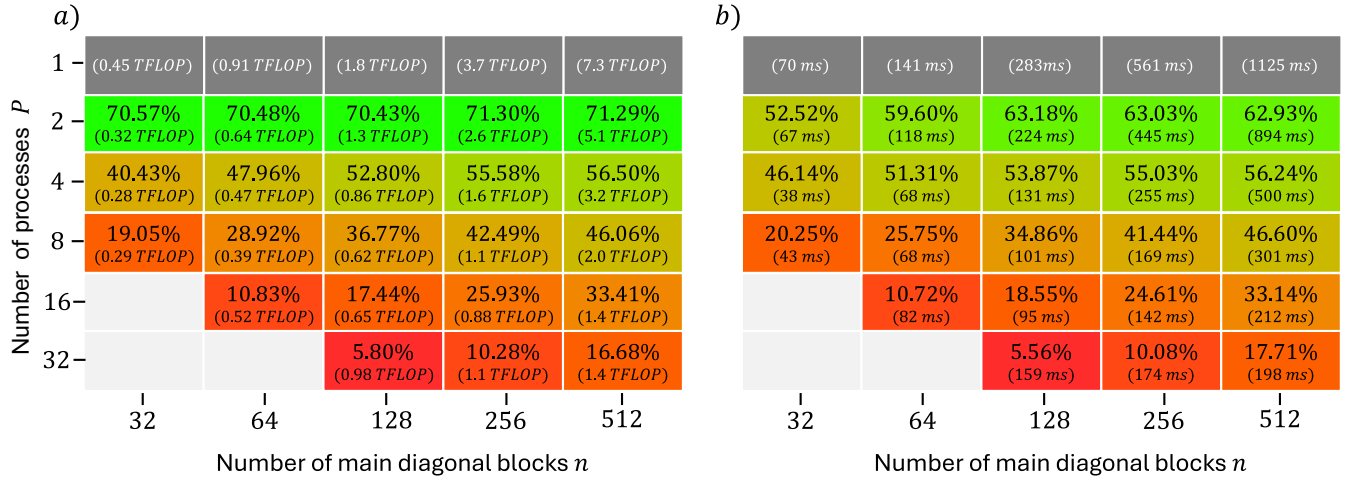


Figure 4: a) Theoretical maximum parallel efficiency of the complete selected-inversion procedure (PPOBTAF + POBTARSSI + PPOBTASI) as a function of the number of main diagonal blocks (horizontal axis) and processes (vertical axis) for BTA matrices with $b=1024$ and $a=256$. b) Experimental parallel efficiency of the complete selected-inversion procedure (PPOBTAF + POBTARSSI + PPOBTASI) using the theoretically determined ideal load balancing factor r_{LB} .

the ratio between the reduced system’s size and each partition is the most advantageous. For the same reason, fewer processes lead to greater parallel efficiency.

5 Evaluation

We implement the methods described in Section 3 and evaluate their performances. First, we measure the parallel efficiency of our methods on a synthetic dataset, giving an overview of our method’s performances. Then, we perform a weak scaling analysis for both the block-sequential and nested-solving approaches for solving the reduced system. Finally, we showcase a comparison of our methods, against the state-of-the-art sparse direct solvers MUMPS and PARDISO. We will refer to *BTA-density* the density of non-zeros elements within the BTA sparsity pattern of a sparse matrix.

5.1 Implementation

We implement all block-sequential and parallel algorithms in Python, using NumPy[22] on CPU and CuPy [37] on GPU to interface with optimized BLAS/LAPACK libraries. Our code utilizes MPI with mpi4py [14], GPU-aware if available, but also the NVIDIA Collective Communications Library (NCCL) [2, 3, 7, 45, 49] on machines equipped with NVLink for direct inter-GPU communication. We employ one (MPI) process per CPU or GPU chip (socket). As described in Section 4, our implementations replace many of the TRSM operations appearing in Algorithms 4 and 6 by GEMM calls, which exhibit much higher performance in the utilized BLAS libraries. We use Reduce, Gather, and Scatter collectives (and their all-variants) to assemble the reduced system in the root process (or a subset of processes in the case of nested solving), perform its selected inversion, and scatter back the results, resulting in a gather-scatter communication strategy.

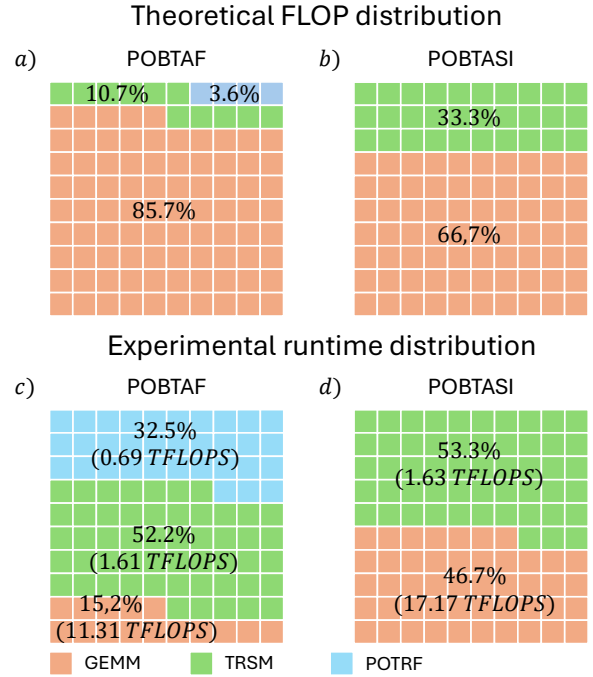


Figure 5: Theoretical FLOP count distributions for the GEMM, TRSM, and POTRF routines within the a) POBTAF and b) POBTASI algorithms. c) and d) report the corresponding breakdown based on actual runtime measurements for a BTA matrix with $b = 1024$ and $a = 256$ on an NVIDIA GH200 (GPU). We show the kernel performances in TFLOPS in parentheses.

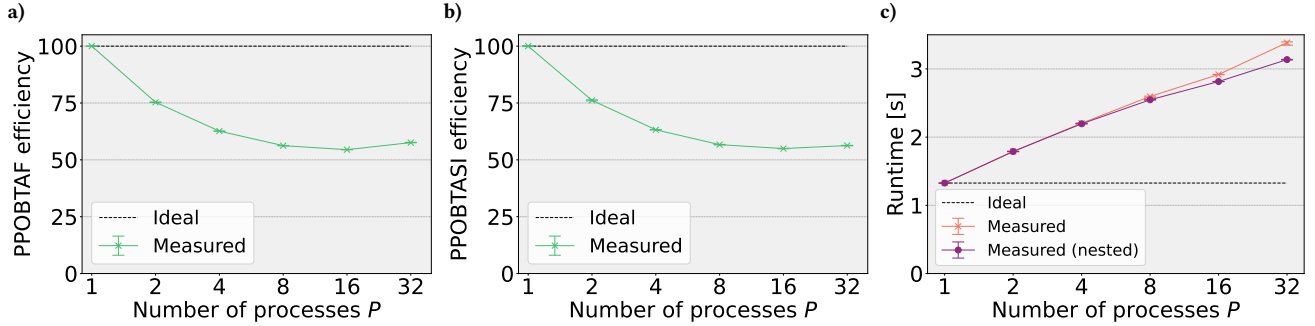


Figure 6: Weak-scaling results for the parallel selected-inversion algorithm on the Alps supercomputer from 1 to 32 processes (GPUUs). a) Efficiency obtained for the PPOBTAF routine (parallel Cholesky factorization). b) Same as a), but for the PPOBTASI function (parallel selected inversion). c) Time-to-solution of the complete parallel approach. The solid lines refer to actual measurements; the dashed lines represent the ideal efficiency and runtime behavior.

5.2 Experimental setup

We perform experiments using four different BTA datasets. First, we measure the parallel efficiency of our codes using a synthetic dataset, (1), that spans a wide range of problem sizes: $n \in \{32, 64, 128, 256, 512\}$, $b = 1024$, and $a = 256$, giving an overview of the efficiency of our methods. Then, we employ two datasets, (2) and (3), based on precision matrices arising from statistical modeling in air temperature prediction using the INLA method, specifically: $n = 365$, $b = 2865$, $a = 4$ and $n = 250$, $b = 4002$, $a = 6$. Dataset (2) is presented in 3 different BTA densities, representing different mesh connectivities: $d \in \{0.69\%, 3\%, 5\%\}$. Dataset (3) presents a BTA-density $d = 0.52\%$. The overall densities of these sparse matrices vary between 0.006% and 0.041%. See Fig. 1 for a visual representation. Finally, we construct a fourth dataset (4) to perform a weak scaling analysis. This dataset is based on the same sparse precision matrix as dataset (2), but here we devise a per-process temporal discretization over one quarter of a year, i.e., 90 days, so that the partition size is $n_p = 90$ before considering load balancing.

More precisely, each dataset contains the following BTA matrices:

- (1) $n \in \{32, 64, 128, 256, 512\}$, $b = 1024$, $a = 256$
- (2) $n = 365$, $b = 2865$, $a = 4$, $d \in \{0.69\%, 3\%, 5\%\}$,
- (3) $n = 250$, $b = 4002$, $a = 6$, $d = 0.52\%$
- (4) $n \in \{90, 180, 360, 720, 1440, 2880\}$, $b = 2865$, $a = 4$

We perform our CPU experiments on the Fritz cluster of the Erlangen National High Performance Computing Center (NHR@FAU). We utilize the spr1tb partition, where each node is equipped with 2 52-core Intel Xeon Platinum 8470 (Sapphire Rapids) CPUs. The nodes are connected to an Infiniband network. We run our GPU experiments on the Alps supercomputer of the Swiss National Supercomputing Center (CSCS). Each compute node comprises four NVIDIA GH200 Superchips.

The Grace CPU has 72 Arm Neoverse V2 cores, while the Hopper GPU, on which our code runs, has a maximum theoretical performance of 34 TFLOPS with the regular double-precision floating-point units and 67 TFLOPS when using the double-precision tensor cores. Each Superchip has 128GB LPDDR5X and 96GB HMB3 memory.

All nodes are connected using an HPC Cray Slingshot-11 network with 200 Gbps injection bandwidth per Superchip. Intra-Superchip and Inter-GPU (up to 256 GPUUs) communication relies on NVLink with 900GB/s bandwidth. All operations are done in double precision. All runtimes presented are median values out of 10 executions, while the error bars correspond to the 95% confidence intervals.

5.3 Experimental parallel efficiency

Using dataset (1), we measure the experimental parallel efficiency of the entire distributed selected-inversion procedure for different P and n values, but constant $b = 1024$ and $a = 256$, and present it in Fig. 4.b). We compute the efficiency as the ratio of parallel runtime to the block-sequential execution. The runtimes in parentheses are median values out of 20 measurements.

We make the following observations with respect to the theoretical efficiency in Fig. 4.a). The two-process efficiency is about 10% lower than expected. This difference could be attributed to the fact that communication is not considered in our theoretical analysis. However, we do not observe such discrepancies across the board. As we run our algorithms using the theoretical load balancing computed in 4, by profiling the execution, we find that for $P = 2$ and $n = 512$, the PPOBTAF runtime is 475 ms, and the middle process spends about 180 ms waiting for the top process, implying that the theoretically determined ideal load balancing factor of 2.25 is sub-optimal. We further discuss this sub-optimal load balancing in the following paragraph.

5.3.1 Discussion on the load balancing. The experimental results differ from the theoretical ones, partially due to sub-optimal load balancing. Here, we reiterate that in typical scientific problems, a and b do not grow arbitrarily large. They take instead relatively small values, which pose a challenge in predicting the performance of BLAS- and LAPACK-based implementations because matrix-matrix multiplication exposes higher parallelism than triangular routines such as POTRF and TRSM. This issue is further exacerbated in state-of-the-art GPU accelerators, where vendor-optimized GEMM implementations may use specialized matrix-product units (tensor cores) efficiently. To provide a concrete example, we show

in Fig. 5.a) and b) the theoretical FLOP count distribution of the GEMM, TRSM, and POTRF routines for POBTAF and POBTASI, using $b = 1024$ and $a = 256$. Both methods appear to be dominated by the GEMM operations. However, when we measure the actual performance, we observe that most of the runtime is spent on TRSM and POTRF, which perform poorly relative to GEMM. The kernels’ runtime breakdown and performance in TFLOPS on GH200’s GPU are given in Fig. 5.c) and d). POTRF’s runtime ratio in POBTAF is 32.5%. Since increasing the top partition’s workload translates into increased POTRF calls, the theoretically optimal load balancing ratio may differ significantly from the practically optimal one. For these reasons, we decided to fine-tune the load balancing factor that we use in Section 5.5 with respect to the given problem and hardware. To conclude, although fine-tuning the load-balancing ratio to specific problem sizes is, of course, feasible, it would be preferable to identify means to automatically derive better ratios for any parameters. It poses a direction for future work.

5.4 Weak scaling

We perform weak-scaling experiments on the Alps supercomputer using dataset (4) and present the results in Fig. 6. The left (middle) subfigures show PPOBTAF’s (PPOBTASI’s) speedup and efficiency. The parallel methods exhibit almost perfect scaling, except for an efficiency loss from 1 to 2 processes. The block-sequential POBTAF runs for 2.51s, while PPOBTAF’s execution with two processes takes 1.56s, of which about 120ms is the latency of an Allreduce operation with NCCL. Furthermore, the middle process spends 200ms waiting for the top process, pointing again to sub-optimal load balancing. We present in the right subfigure the total runtime for the parallel selected-inversion operation with and without nested solving. As, with 90 diagonal blocks per process, dataset (4) is large, the nested solving’s communication overhead is relatively small compared to the added computational cost, leading to a performance improvement for 16 and 32 processes. The observed parallel efficiency is 47.2% and 42.3% at 16 and 32 GPUs, respectively. As datasets (1-3) are much smaller, the nested solving approach does not bring any performance gains and, therefore, we do not present it further.

5.5 Comparison to State-of-the-Art

We use datasets (2) and (3) to compare Serinv performances against the state-of-the-art sparse direct solvers PARDISO (version 7.2) and MUMPS (version 5.7.3). To provide a fair comparison, the sparse solvers utilize the true underlying sparsity pattern of the matrix and not its block-dense version. Both libraries provide factorization and selected matrix inversion routines for general sparse matrices and, therefore, also support BTA sparsity patterns. These libraries rely on METIS/ParMETIS [25] for providing suitable matrix permutations to minimize fill-in during the factorization. Their complete selected inversion routines can, therefore, be split into three distinct phases: symbolic factorization, numerical factorization, and selected inversion. The first phase only needs to be performed once per sparsity pattern, allowing the amortization of its cost when for matrices with recurrent sparsity patterns. We, therefore, omit the inclusion of the analysis phase in the reported runtimes. The PARDISO library supports shared-memory parallelism, while MUMPS also offers a distributed-memory implementation. However, neither

of them offers GPU implementations of their sparse routines. After testing the libraries’ performances, we found the best configuration for each of them to be: 32 OpenMP/MKL threads for PARDISO and 52 for MUMPS and Serinv-CPU. Furthermore, following MUMPS’s documentation [1], we found that MUMPS performs best when operating on blocks of 2048 columns at a time, and we set the ICNTL(27) parameter appropriately.

As discussed in Section 5.3.1, we experimentally adjust the load balancing factor used in the multi-process runs of Serinv, where we found a ratio of about 1.8 to be optimal. We found PARDISO to be the fastest available library in literature, and thus present in Figure 7 the strong-scaling speedup of MUMPS and Serinv relative to the best performance achieved by PARDISO. The speedup results presented in Figure 7 encompass the factorization and selected inversion phases of the matrix from dataset (2) and its different BTA-density declination. For all three variations of BTA-density, Serinv-CPU (resp. Serinv-GPU) exhibits the same runtime, as the in-block density doesn’t affect the operations performed. The sparse implementation of PARDISO can leverage lower densities to its advantage, outperforming Serinv-CPU’s single-node version. We can, however, see from Figure 7 that already from a BTA-density of 3%, Serinv’s single node CPU implementation outperforms PARDISO, leveraging its adaption to the BTA sparsity pattern. Serinv-CPU (resp. GPU) achieves a strong scaling parallel efficiency of 28.9% (resp. 32.9%) on dataset (2) initial matrix, leading to a speedup of 4.63 (resp. 5.17) over its single-process implementation.

In Fig. 8, we present a breakdown of the runtimes for the factorization and selected inversion of the matrix from dataset (3), as well as their combined runtimes. We observe that MUMPS’s factorization routine is performant and scalable, outperforming Serinv-CPU and PARDISO for any number of processes. However, MUMPS’ selected inversion takes about an order of magnitude longer than the two other CPU variants, making it the least-suited method to perform selected inversion on sparse BTA matrices. Both sparse solvers outperform Serinv-CPU during the factorization phase. Conversely, for the selected inversion routine, Serinv-CPU outperforms MUMPS even on a single process and PARDISO from 2 processes on. The combined runtimes make PARDISO, up to 4 MPI processes, the fastest CPU solver. Serinv-CPU scales further to 16 MPI processes, providing the best overall time-to-solution for a CPU solver with 55.09 seconds, PARDISO (resp. MUMPS) taking 145.14 (resp. 729.2) seconds. The single-process GPU implementation of Serinv outperforms all CPU variants for both the factorization and selected inversion phases, achieving 4.62 times speedup over MUMPS’ factorization and 21.95 times speedup over PARDISO’ selected inversion. Serinv-GPU provides, in all cases, the fastest factorization, selected inversion, and time-to-solution.

We conclude that even for very sparse BTA matrices, Serinv-CPU already provides comparable performance to PARDISO. When increasing the BTA density above 3%, Serinv-CPU becomes the most efficient option. Serinv-GPU outperforms all CPU solvers by one to two orders of magnitudes depending on the configuration (71.4 times speedup over PARDISO and 380.9 times speedup over MUMPS on dataset (3)).

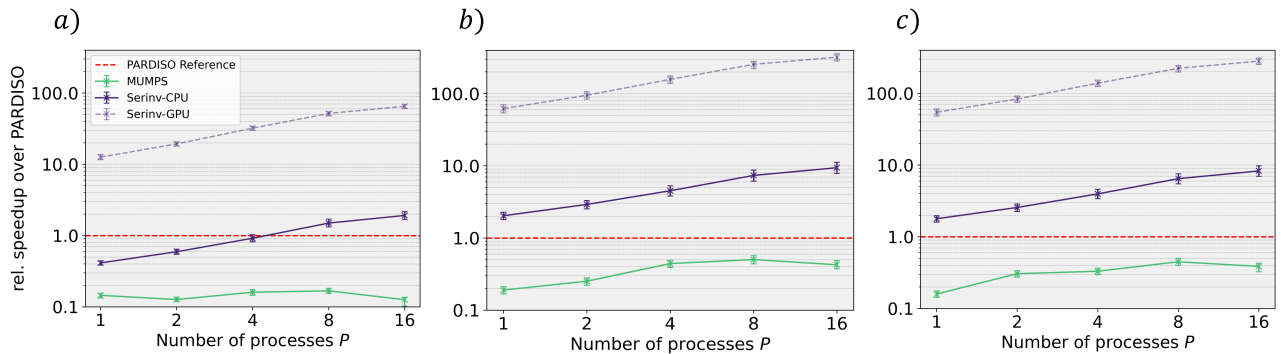


Figure 7: Relative speedup for selected matrix inversion (including factorization phase) of MUMPS, Serinv-CPU, and Serinv-GPU using an increasing number of processes over the best multithreaded PARDISO configuration (32 threads). The dataset (2) and its BTA-density declinations are used, leading from left to right: a) Dataset (2), with 0.7% BTA-density. b) Dataset (2), with 3% BTA-density. c) Dataset (2), with 5% BTA-density. CPU codes run on the Fritz cluster and Serinv-GPU on the Alps supercomputer.

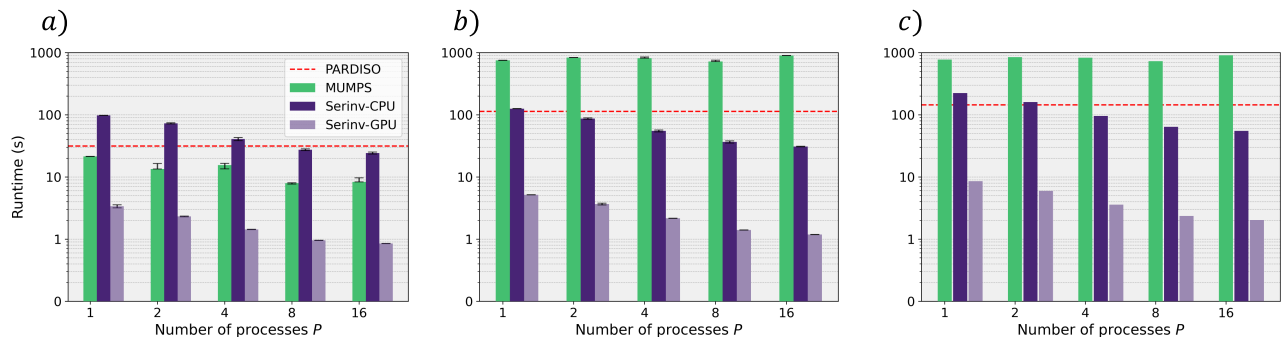


Figure 8: Runtime breakdown in Factorization and Selected Inversion of PARDISO and strong-scaling of MUMPS, Serinv-CPU, and Serinv-GPU with an increasing number of nodes over the best multithreaded PARDISO configuration (32 threads). a) factorization runtime, b) selected inversion runtime, and c) total time-to-solution a) + b). CPU codes run on the Fritz cluster and Serinv-GPU on the Alps supercomputer.

6 Conclusion

We derived novel parallel algorithms for the selected inversion of positive semi-definite BTA matrices and implemented them in the scalable, GPU-accelerated *Serinv* library. We conducted a theoretical analysis of the proposed methods and evaluated our implementations on synthetics and real datasets. We first demonstrated weak scaling efficiency of 47.2% when going from 1 to 16 GPUs. We then conducted a comparison of *Serinv*'s performances against the state-of-the-art sparse solvers PARDISO and MUMPS for which we show up to 2.6x (resp. 71.4x) speedup on CPU backend (resp. GPU) over PARDISO and 14.0x (resp. 380.9x) speedup over MUMPS when scaling to 16 processes (resp. GPUs). Future work may include: (i) further theoretical study, especially regarding nested solving, to uncover better scaling opportunities; (ii) usage of heuristics to quickly determine better load-balancing ratios tailored to the exact problem parameters; and (iii) investigation of custom kernels that combine executions of POBTAF, GEMM, and TRSM to accelerate the intra-device execution. Finally, the proposed distributed selected-inversion algorithms have the ability to extend the feasible

scale of important materials science and climate modeling applications on state-of-the-art supercomputers, enabling new scientific discoveries.

Acknowledgments

This work received funding from the Swiss National Science Foundation (SNSF) under the grant agreements “Quantum Transport Simulations at the Exascale and Beyond (QuaTrEx)” (n0 209358). We acknowledge support and HPC resources provided by the Swiss National Supercomputing Center (CSCS) under project lp16 as well as the Erlangen National High Performance Computing Center (NHR@FAU) of the Friedrich-Alexander-Universität Erlangen-Nürnberg (FAU) under the NHR project 80227.

References

- [1] 2024. Multifrontal Massively Parallel Solver (MUMPS 5.7.3) Users' guide. https://mumps-solver.org/doc/userguide_5.7.3.pdf
- [2] 2024. NVIDIA Collective Communication Library (NCCL) Documentation – NCCL 2.23.4 documentation. <https://docs.nvidia.com/deeplearning/nccl/user-guide/docs/index.html>

- [3] 2024. NVIDIA/ncll. <https://github.com/NVIDIA/ncll> original-date: 2015-11-14T00:12:04Z.
- [4] P. R. Amestoy, I. S. Duff, and J. Y. L'Excellent. 2000. Multifrontal parallel distributed symmetric and unsymmetric solvers. *Computer Methods in Applied Mechanics and Engineering* 184, 2 (April 2000), 501–520. [https://doi.org/10.1016/S0045-7825\(99\)00242-X](https://doi.org/10.1016/S0045-7825(99)00242-X)
- [5] Patrick R. Amestoy, Iain S. Duff, Jean-Yves L'Excellent, and Jacko Koster. 2001. A Fully Asynchronous Multifrontal Solver Using Distributed Dynamic Scheduling. *SIAM J. Matrix Anal. Appl.* 23, 1 (Jan. 2001), 15–41. <https://doi.org/10.1137/S0895479899358194> Publisher: Society for Industrial and Applied Mathematics.
- [6] Patrick R. Amestoy, Iain S. Duff, Jean-Yves L'Excellent, and Jacko Koster. 2001. MUMPS: A General Purpose Distributed Memory Sparse Solver. In *Applied Parallel Computing. New Paradigms for HPC in Industry and Academia*, Tor Sorevik, Fredrik Manne, Assefaw Hadish Gebremedhin, and Randi Moe (Eds.). Springer, Berlin, Heidelberg, 121–130. https://doi.org/10.1007/3-540-70734-4_16
- [7] Ammar Ahmad Awan, Ching-Hsiang Chu, Hari Subramoni, and Dhableswar K. Panda. 2018. Optimized Broadcast for Deep Learning Workloads on Dense-GPU InfiniBand Clusters: MPI or NCCL?. In *Proceedings of the 25th European MPI Users' Group Meeting* (Barcelona, Spain) (*EuroMPI '18*). Association for Computing Machinery, New York, NY, USA, Article 2, 9 pages. <https://doi.org/10.1145/3236367.3236381>
- [8] P A Belov, E R Nugumanov, and S L Yakovlev. 2017. The arrowhead decomposition method for a block-tridiagonal system of linear equations. *Journal of Physics: Conference Series* 929, 1 (nov 2017), 012035. <https://doi.org/10.1088/1742-6596/929/1/012035>
- [9] Matthias Bollhöfer, Olaf Schenk, Radim Janalik, Steve Hamm, and Kiran Gullapalli. 2020. State-of-the-Art Sparse Direct Solvers. In *Parallel Algorithms in Computational Science and Engineering*, Ananth Grama and Ahmed H. Sameh (Eds.). Springer International Publishing, Cham, 3–33. https://doi.org/10.1007/978-3-030-43736-7_1
- [10] S. Bondeli and W. Gander. 1994. Cyclic Reduction for Special Tridiagonal Systems. *SIAM J. Matrix Anal. Appl.* 15, 1 (Jan. 1994), 321–330. <https://doi.org/10.1137/S0895479891220533> Publisher: Society for Industrial and Applied Mathematics.
- [11] Mauro M. Calderara. 2016. *SplitSolve, an Algorithm for Ab-Initio Quantum Transport Simulations*. Doctoral Thesis. ETH Zurich. <https://doi.org/10.3929/ethz-a-010781848> Accepted: 2017-09-22T13:18:14Z.
- [12] Stephen Cauley, Jitesh Jain, Cheng-Kok Koh, and Venkataraman Balakrishnan. 2007. A scalable distributed method for quantum-scale device simulation. *Journal of Applied Physics* 101, 12 (June 2007), 123715. <https://doi.org/10.1063/1.2748621>
- [13] Stephen Cauley, Mathieu Luisier, Venkataraman Balakrishnan, Gerhard Klimeck, and Cheng-Kok Koh. 2011. Distributed non-equilibrium Green's function algorithms for the simulation of nanoelectronic devices with scattering. *Journal of Applied Physics* 110, 4 (Aug. 2011), 043713. <https://doi.org/10.1063/1.3624612>
- [14] Lisandro Dalcin, Rodrigo Paz, and Mario Storti. 2005. MPI for Python. *J. Parallel and Distrib. Comput.* 65, 9 (2005), 1108–1115. <https://doi.org/10.1016/j.jpdc.2005.03.010>
- [15] James W. Demmel, Nicholas J. Higham, and Robert S. Schreiber. 1995. Stability of block LU factorization. *Numerical Linear Algebra with Applications* 2, 2 (1995), 173–190. <https://doi.org/10.1002/nla.1680020208> arXiv:<https://onlinelibrary.wiley.com/doi/pdf/10.1002/nla.1680020208>
- [16] AM Erisman and WF Tinney. 1975. On computing certain elements of the inverse of a sparse matrix. *Commun. ACM* 18, 3 (1975), 177–179.
- [17] Lisa Gaedke-Merzhäuser. 2024. *lisa-gm/INLA_DIST*. https://github.com/lisa-gm/INLA_DIST original-date: 2021-04-14T07:35:36Z.
- [18] Lisa Gaedke-Merzhäuser, Elias Krainski, Radim Janalik, Håvard Rue, and Olaf Schenk. 2024. Integrated Nested Laplace Approximations for Large-Scale Spatiotemporal Bayesian Modeling. *SIAM Journal on Scientific Computing* 46, 4 (2024), B448–B473. <https://doi.org/10.1137/23M1561531>
- [19] Lisa Gaedke-Merzhäuser, Janet van Niekerk, Olaf Schenk, and Håvard Rue. 2023. Parallelized integrated nested Laplace approximations for fast Bayesian inference. *Statistics and Computing* 33, 25 (2023). [10.1007/s11222-022-10192-1](https://doi.org/10.1007/s11222-022-10192-1).
- [20] Alan George, Micheal T Heath, Esmond Ng, and Joseph Liu. 1987. Symbolic Cholesky factorization on a local-memory multiprocessor. *Parallel Comput.* 5, 1 (1987), 85–95. [https://doi.org/10.1016/0167-8191\(87\)90009-3](https://doi.org/10.1016/0167-8191(87)90009-3) Proceedings of the International Conference on Vector and Parallel Computing-Issues in Applied Research and Development.
- [21] Lukas Gianinazzi, Alexandros Nikolaos Ziogas, Langwen Huang, Piotr Luczynski, Saleh Ashkboosh, Florian Scheidl, Armon Carigiet, Chio Ge, Nabil Abubaker, Maciej Besta, Tal Ben-Nun, and Torsten Hoeftler. 2024. Arrow Matrix Decomposition: A Novel Approach for Communication-Efficient Sparse Matrix Multiplication. In *Proceedings of the 29th ACM SIGPLAN Annual Symposium on Principles and Practice of Parallel Programming* (Edinburgh, United Kingdom) (*PPoPP '24*). Association for Computing Machinery, New York, NY, USA, 404–416. <https://doi.org/10.1145/3627535.3638496>
- [22] Charles R. Harris, K. Jarrod Millman, Stéfan J. van der Walt, Ralf Gommers, Pauli Virtanen, David Cournapeau, Eric Wieser, Julian Taylor, Sebastian Berg, Nathaniel J. Smith, Robert Kern, Matti Picus, Stephan Hoyer, Marten H. van Kerkwijk, Matthew Brett, Allan Haldane, Jaime Fernández del Río, Mark Wiebe, Pearu Peterson, Pierre Gérard-Marchant, Kevin Sheppard, Tyler Reddy, Warren Weckesser, Hameer Abbasi, Christoph Gohlke, and Travis E. Oliphant. 2020. Array programming with NumPy. *Nature* 585, 7825 (Sept. 2020), 357–362. <https://doi.org/10.1038/s41586-020-2649-2>
- [23] Don Heller. 1976. Some Aspects of the Cyclic Reduction Algorithm for Block Tridiagonal Linear Systems. *SIAM J. Numer. Anal.* 13, 4 (1976), 484–496. <https://www.jstor.org/stable/2156240> Publisher: Society for Industrial and Applied Mathematics.
- [24] Fagan J K Takahashi, Chin M. 1973. Formation of sparse bus impedance matrix and its application to short circuit study. *Proceedings of the 8th PICA Conference* (1973).
- [25] George Karypis and Vipin Kumar. 1998. A fast and high quality multilevel scheme for partitioning irregular graphs. *SIAM Journal on scientific Computing* 20, 1 (1998), 359–392. [10.5555/305219.305248](https://doi.org/10.5555/305219.305248).
- [26] S. Li, S. Ahmed, G. Klimeck, and E. Darve. 2008. Computing entries of the inverse of a sparse matrix using the FIND algorithm. *J. Comput. Phys.* 227, 22 (Nov. 2008), 9408–9427. <https://doi.org/10.1016/j.jcp.2008.06.033>
- [27] S. Li and E. Darve. 2009. Optimization of the FIND Algorithm to Compute the Inverse of a Sparse Matrix. In *2009 13th International Workshop on Computational Electronics*. 1–4. <https://doi.org/10.1109/IWCE.2009.5091136>
- [28] S. Li and E. Darve. 2012. Extension and optimization of the FIND algorithm: Computing Green's and less-than Green's functions. *J. Comput. Phys.* 231, 4 (Feb. 2012), 1121–1139. <https://doi.org/10.1016/j.jcp.2011.05.027>
- [29] S. Li, W. Wu, and E. Darve. 2013. A fast algorithm for sparse matrix computations related to inversion. *J. Comput. Phys.* 242 (June 2013), 915–945. <https://doi.org/10.1016/j.jcp.2013.01.036>
- [30] Lin Lin, Jianfeng Lu, Lexing Ying, Roberto Car, et al. 2009. Fast algorithm for extracting the diagonal of the inverse matrix with application to the electronic structure analysis of metallic systems. *Commun. Math. Sci.* 7, 1 (2009), 755–777.
- [31] Lin Lin, Chao Yang, Juan C. Meza, Jianfeng Lu, Lexing Ying, and Weina E. 2011. SellInV—An Algorithm for Selected Inversion of a Sparse Symmetric Matrix. *ACM Trans. Math. Softw.* 37, 4, Article 40 (feb 2011), 19 pages. <https://doi.org/10.1145/1916461.1916464>
- [32] Finn Lindgren, Haakon Bakka, David Bolin, Elias Krainski, and Håvard Rue. 2024. A diffusion-based spatio-temporal extension of Gaussian Matérn fields. *SORT-Statistics and Operations Research Transactions* (2024), 3–66.
- [33] Finn Lindgren, Håvard Rue, and Johan Lindström. 2011. An explicit link between Gaussian fields and Gaussian Markov random fields: the stochastic partial differential equation approach. *Journal of the Royal Statistical Society: Series B (Statistical Methodology)* 73, 4 (2011), 423–498. [10.1111/j.1467-9868.2011.00777.x](https://doi.org/10.1111/j.1467-9868.2011.00777.x).
- [34] M. Louter-Nool. 1992. Block-Cholesky for parallel processing. *Applied Numerical Mathematics* 10, 1 (Jan. 1992), 37–57.
- [35] Mathieu Luisier and Gerhard Klimeck. 2008. OMEN an Atomistic and Full-Band Quantum Transport Simulator for post-CMOS Nanodevices. In *2008 8th IEEE Conference on Nanotechnology*. 354–357. <https://doi.org/10.1109/NANO.2008.110>
- [36] Mathieu Luisier, Andreas Schenk, and Wolfgang Fichtner. 2006. Quantum transport in two- and three-dimensional nanoscale transistors: Coupled mode effects in the nonequilibrium Green's function formalism. *Journal of Applied Physics* 100, 4 (08 2006), 043713. <https://doi.org/10.1063/1.2244522> arXiv:https://pubs.aip.org/aip/jap/article-pdf/doi/10.1063/1.2244522/7892769/043713_1_online.pdf
- [37] Ryoosuke Okuta, Yuya Unno, Daisuke Nishino, Shohei Hido, and Crissman Loomis. 2017. CuPy: A NumPy-Compatible Library for NVIDIA GPU Calculations. In *Proceedings of Workshop on Machine Learning Systems (LearningSys) in The Thirty-first Annual Conference on Neural Information Processing Systems (NIPS)*. http://learningsys.org/nips17/assets/papers/paper_16.pdf
- [38] Dan Erik Petersen, Song Li, Kurt Stokbro, Hans Henrik B. Sørensen, Per Christian Hansen, Stig Skelboe, and Eric Darve. 2009. A hybrid method for the parallel computation of Green's functions. *J. Comput. Phys.* 228, 14 (Aug. 2009), 5020–5039. <https://doi.org/10.1016/j.jcp.2009.03.035>
- [39] Dan Erik Petersen, Hans Henrik B. Sørensen, Per Christian Hansen, Stig Skelboe, and Kurt Stokbro. 2008. Block tridiagonal matrix inversion and fast transmission calculations. *J. Comput. Phys.* 227, 6 (March 2008), 3174–3190. <https://doi.org/10.1016/j.jcp.2007.11.035>
- [40] Eric Polizzi and Ahmed H. Sameh. 2006. A parallel hybrid banded system solver: the SPIKE algorithm. *Parallel Comput.* 32, 2 (Feb. 2006), 177–194. <https://doi.org/10.1016/j.parco.2005.07.005>
- [41] Håvard Rue, Sara Martino, and Nicolas Chopin. 2009. Approximate Bayesian inference for latent Gaussian models by using integrated nested Laplace approximations. *Journal of the Royal Statistical Society Series B: Statistical Methodology* 71, 2 (2009), 319–392.
- [42] Olaf Schenk and Klaus Gärtner. 2004. Solving unsymmetric sparse systems of linear equations with PARDISO. *Future Generation Computer Systems* 20, 3 (April 2004), 475–487. <https://doi.org/10.1016/j.future.2003.07.011>
- [43] Olaf Schenk and Klaus Gärtner. 2006. On fast factorization pivoting methods for sparse symmetric indefinite systems. *ETNA. Electronic Transactions on Numerical Analysis [electronic only]* 23 (2006), 158–179. <http://eudml.org/doc/127439>

- [44] Olaf Schenk, Klaus Gärtner, Wolfgang Fichtner, and Andreas Stricker. 2001. PAR-DISO: a high-performance serial and parallel sparse linear solver in semiconductor device simulation. *Future Generation Computer Systems* 18, 1 (Sept. 2001), 69–78. [https://doi.org/10.1016/S0167-739X\(00\)00076-5](https://doi.org/10.1016/S0167-739X(00)00076-5)
- [45] Daniele De Sensi, Lorenzo Pichetti, Flavio Vella, Tiziano De Matteis, Zebin Ren, Luigi Fusco, Matteo Turisini, Daniele Cesarini, Kurt Lust, Animesh Trivedi, Duncan Roweth, Filippo Spiga, Salvatore Di Girolamo, and Torsten Hoefer. 2024. Exploring GPU-to-GPU Communication: Insights into Supercomputer Interconnects. <https://doi.org/10.48550/arXiv.2408.14090> arXiv:2408.14090.
- [46] Louise Spellacy and Darach Golden. 2018. Partial Inverses of Complex Block Tridiagonal Matrices. In *Parallel Processing and Applied Mathematics*, Roman Wyrzykowski, Jack Dongarra, Ewa Deelman, and Konrad Karczewski (Eds.). Springer International Publishing, Cham, 634–645. https://doi.org/10.1007/978-3-319-78024-5_55
- [47] A. Svizhenko, M. P. Anantram, T. R. Govindan, B. Biegel, and R. Venugopal. 2002. Two-dimensional quantum mechanical modeling of nanotransistors. *Journal of Applied Physics* 91, 4 (Feb. 2002), 2343–2354. <https://doi.org/10.1063/1.1432117>
- [48] I. E. Venetis, A. Kouris, A. Sobczyk, E. Gallopoulos, and A. H. Sameh. 2015. A direct tridiagonal solver based on Givens rotations for GPU architectures. *Parallel Comput.* 49 (Nov. 2015), 101–116. <https://doi.org/10.1016/j.parco.2015.03.008>
- [49] Cliff Woolley. [n. d.]. NCCL: ACCELERATED MULTI-GPU COLLECTIVE COMMUNICATIONS. ([n. d.]). <https://images.nvidia.com/events/sc15/pdfs/NCCL-Woolley.pdf>
- [50] Andrew Zammit-Mangion and Jonathan Rougier. 2018. A sparse linear algebra algorithm for fast computation of prediction variances with Gaussian Markov random fields. *Computational Statistics & Data Analysis* 123 (2018), 116–130. [10.1016/j.csda.2018.02.001](https://doi.org/10.1016/j.csda.2018.02.001).
- [51] Alexandros Nikolaos Ziogas, Tal Ben-Nun, Guillermo Indalecio Fernández, Timo Schneider, Mathieu Luisier, and Torsten Hoefer. 2019. A data-centric approach to extreme-scale ab initio dissipative quantum transport simulations. In *Proceedings of the International Conference for High Performance Computing, Networking, Storage and Analysis (Denver, Colorado) (SC '19)*. Association for Computing Machinery, New York, NY, USA, Article 1, 13 pages. <https://doi.org/10.1145/3295500.3357156>